International Journal of Hydrogen Energy 65 (2024) 769–778

Contents lists available at ScienceDirect

International Journal of Hydrogen Energy

journal homepage: www.elsevier.com/locate/he

Boosting dehydrogenation of dodecahydro-N-ethylcarbazole over Pd nanoclusters with tailored electronic structures loaded on nitrogen-doped carbon

Yumo Li [1], Jikai Ye [1], Tian Xu, Guanglin Xia [*], Xuebin Yu [**]

Department of Materials Science, Fudan University, Shanghai, 200433, China

ARTICLE INFO

Keywords:
Hydrogen storage
Liquid organic hydrogen carriers
N-ethylcarbazole
Dehydrogenation

ABSTRACT

Dodecahydro-N-ethylcarbazole (12H-NEC) is considered as a highly promising liquid organic hydrogen carrier, but its commercial application is constrained by the requirement of large amounts of precious metal catalysts for dehydrogenation. Herein, Pd nanoclusters with an average particle size of 1.1 nm supported on amine groups modified carbon blacks (Pd/N–C_{HNO3}) are developed to efficiently catalyze the dehydrogenation of 12H-NEC with a low loading of Pd (2.2 wt%, 0.12 mol%). Induced by the nitrogen doping in the carbon black, the *d*-band center of the Pd (111) surface shifts from −1.64 eV to −1.53 eV, resulting in the electron-deficient structure of thus-formed Pd nanoclusters owing to the electron transfer from Pd to N atoms and uniform distribution of Pd nanoclusters inside of carbon blacks. This electron transfer effectively tunes Pd^0:$Pd^{\delta+}$ ratio for enhancing the adsorption of reactant species of 12H-NEC on the surface of Pd nanoclusters and hence facilitates the catalytic role of Pd nanoclusters in enhancing the hydrogen desorption performance of 12H-NEC. As a result, every step of the dehydrogenation of 12H-NEC under the catalysis of Pd nanoclusters on the nitrogen-doped support exhibits lower ΔG values compared to the non-doped support, which provides direct evidence to the important role of the nitrogen doping of the catalyst support in improving the dehydrogenation performance of 12H-NEC on the Pd surface. Therefore, a hydrogen release capacity of 5.60 wt% with 100% conversion and a selectivity of 90% could be obtained for 12H-NEC under the catalysis of Pd nanoclusters supported on amine-functionalized carbon black at 453 K with a low precious metal dosage (0.12 mol%).

1. Introduction

Hydrogen is considered as one of the most promising clean energy sources due to its zero carbon emissions and environmental friendliness [1,2]. However, the low density of hydrogen gas poses significant challenges to its storage and transportation that limit the large-scale commercialization of hydrogen energy. In the transportation of hydrogen over long distances, the cost of transporting hydrogen in the form of high-pressure hydrogen gas cylinders *via* railroads is high [3,4] and the hydrogen embrittlement phenomenon has made it hard to transport hydrogen through pipelines [5,6]. Therefore, the development of effective and safe strategies for high-weight and high-volume density hydrogen storage are crucial to overcoming this limitation and promoting the widespread commercial application of hydrogen energy. Compared with other hydrogen storage manners, liquid organic hydrogen carriers (LOHC) offer several advantages, including high energy density, excellent chemical stability, and environmental friendliness. Moreover, the LOHCs can be well-compatible with existing oil or gas pipelines [7–11], enabling them ideal candidates for addressing the challenges associated with long-distance hydrogen transportation. The transportability of LOHCs at ambient temperature and pressure makes them a promising candidate as onboard hydrogen sources for vehicles [12].

Compared to nitrogen-free aromatic compounds, the hydrides of nitrogen-containing aromatic compounds exhibit superior thermodynamic properties in dehydrogenation reactions. This superiority is attributed to enhanced conjugation resulting from changes in molecular composition [13,14]. Therefore, nitrogen-containing cyclic compounds

* Corresponding author.
** Corresponding author.
E-mail addresses: xiaguanglin@fudan.edu.cn (G. Xia), yuxuebin@fudan.edu.cn (X. Yu).
[1] Yumo Li and Jikai Ye contributed equally to this work.

https://doi.org/10.1016/j.ijhydene.2024.03.367
Received 5 December 2023; Received in revised form 16 March 2024; Accepted 30 March 2024
Available online 10 April 2024

are generally considered potential LOHC materials. Such as 12H-2-(N-Methylbenzyl)pyridine (12H-MBP) has been confirmed that 6.09 wt% of hydrogen can be released at 523 K for 4 h catalyzed by Pd-based or Pt-based catalyst [15,16], and 8H–N-Methylindole (8H–N-MID) can release 5.46 wt% of hydrogen within 8 h at 443 K catalyzed by Pd-based catalyst [17]. Tetrahydroquinoline (THQ) can achieve visible-light-promoted iridium (III)-catalyzed acceptorless dehydrogenation at room temperature and releasing 3.01 wt% of hydrogen [18]. Among these nitrogen-containing cyclic compounds, N-ethylcarbazole (NEC) as a potential LOHC carrier has garnered wide attention due to its low hydrogenation and dehydrogenation temperature (below 473 K), high hydrogen storage density (5.79 wt%), and extremely high hydrogen release purity (99.99%) [19]. The hydrogenation of NEC could be efficiently facilitated by utilizing Ru-based catalysts at temperatures between 403 and 426 K under hydrogen pressures of 5~7 MPa, leading to the formation of 12H-NEC with a purity exceeding 99% [20]. Unfortunately, the complete dehydrogenation of 12H-NEC presents a relatively challenging process that occurs in three steps, each removing two H_2 molecules. This results in the formation of intermediate 8H-NEC and 4H-NEC species, and ultimately leading to the formation of NEC. The transition from 4H-NEC to NEC is considerably slow, impeding the complete dehydrogenation of 12H-NEC [21]. As a result, the dehydrogenation of fully hydrogenated 12H-NEC typically requires the use of noble metals such as Pd or Pt as catalysts, significantly escalating the operational costs of 12H-NEC as a hydrogen carrier.

To mitigate the excessive use of precious metals in dehydrogenation catalysts, many researchers have explored Pd-based and Pt-based catalysts. For instance, the research by Cheng et al. revealed that, among various noble metals (Rh, Pd, Pt, and Au), Pd exhibits the most efficient catalytic performance in the dehydrogenation of 12H-NEC. Pd/Al_2O_3 could realize the complete dehydrogenation of 12H-NEC (5.79 wt%) within 6 h at 453 K but requiring a relatively high Pd loading (0.98 mol %) [22]. To further reduce the amount of Pd catalyst, Fang et al. introduced transition metal Cu as Pd substitutes was proposed by building a bimetallic catalyst on reduced graphene oxides [23]. PdCu/rGO exhibited hydrogen release performance with a Pd loading of 0.23 mol% and realized the complete dehydrogenation. Although the catalysts reported in current literature ensure complete dehydrogenation of 12H-NEC, the catalytic systems employed in these reported studies still exhibit a notable consumption of noble metals (Table S1). In general, it is necessary, but remaining a significant challenge, to reduce the amount of precious metals in the dehydrogenation catalyst while maintaining the effective catalytic effect.

In order to reduce the usage of noble metals in catalysts, it's essential to enhance the catalytic activity of these metals within the catalyst. One potential strategy to enhance catalytic activity involves controlling the particle size of noble metals. It has been widely demonstrated that the catalytic activity of 12H-NEC dehydrogenation catalysts is highly sensitive to the particle size of the active metals within the catalyst. Ma et al. investigated the structure sensitivity at the sub-nanometer scale [24], which confirms that single-atom Pd was not efficient in catalyzing N-ethylcarbazole dehydrogenation because the dehydrogenation of hydrogenated N-ethylcarbazole requires a sufficient number of successive Pd site activations of the reactants. Pd nanoclusters (NCs) with particle sizes of approximately 1~2 nm and an average coordination number of 4.4 exhibited the best catalytic performance [24], which provides insight into the design of catalysts. Another method of enhancing the catalytic performance of the catalyst is to tune the electronic structure of the catalytic metal. The work of Wei et al. suggests that an appropriate ratio of Pd^0 to $Pd^{\delta+}$ in the Pd-based catalyst is favorable for the dehydrogenation of 12H-NEC [25]. In this catalyst, Pd^0 acts as the catalytic active center, accelerating the breaking of C–H bonds during the dehydrogenation process, while $Pd^{\delta+}$ could reduce the adsorption energy of dehydrogenation products.

Previous studies validate that introducing nitrogen doping into the catalyst support to simultaneously anchor metal nanoparticles on the catalyst and tune the electronic structure of the catalyst has been widely applied in various catalysts, such as in electrocatalytic hydrogen evolution or formic acid electrocatalytic oxidation reactions [26–28]. To introduce nitrogen doping to the catalyst support, surface functionalization with APTES emerges as an environmentally benign strategy. In contrast to conventional hydrothermal or pyrolysis methods necessitating heat, this approach facilitates nitrogen incorporation into the catalyst at ambient temperature, finding extensive application in catalyst synthesis. For instance, Qing et al. presented a catalyst featuring PdAu alloy nanoclusters, exhibiting an average particle size of 1.0 nm. These nanoclusters were positioned on APTES-functionalized carbon black, showcasing efficacy in ethanol electrocatalytic oxidation and formic acid dehydrogenation [29]. The introduction of nitrogen doping into catalyst supports could effectively anchor the loaded metal atoms and enhance their dispersion. Meanwhile, the interaction of Pd with nitrogen atoms on the support results in the formation of metal-support interactions based on pyrrolic nitrogen that is able to affect the electronic structure of Pd and enhance its catalytic activity. Due to the electron transfer from Pd to N, introducing a certain proportion of N atoms into the support could effectively tune the ratio of Pd^0 to $Pd^{\delta+}$, which contributes to enhancing the catalytic effect of Pd [30–33]. However, there is currently no report on the adoption of nitrogen-doped supports for improving the catalytic effect of Pd with low loading in promoting the dehydrogenation of 12H-NEC.

Inspired by these research progress, Pd nanoclusters that has an average particle size of 1.1 nm uniformly distributed on nitrogen-doped conductive carbon with nitric acid surface oxidation (denoted as Pd/N–C_{HNO3}), which is realized by the homogeneous molecular chelation between ammine groups and Pd-containing ions, are developed to improve the dehydrogenation of 12H-NEC. Induced by the nitrogen doping in the carbon blacks, the *d*-band center of the Pd (111) surface shifts from −1.64 eV to −1.53 eV and moves closer to the Fermi level, leading to the formation of the electron-deficient structure of thus-formed Pd nanoclusters owing to the electron transfer from Pd to N atoms and the uniform distribution of Pd nanoclusters inside of carbon blacks. Therefore, with a low precious metal dosage (0.12 mol%), a hydrogen release capacity of 5.60 wt% with 100 % conversion and a selectivity of 90% could be obtained for 12H-NEC under the catalysis of Pd/N–C_{HNO3} at 453 K for 8 h. Notably, Pd/N–C_{HNO3} catalysis sustains a 5.49 wt% H_2 release, with 96% capacity retention after five cycles for 40 h. This is attributed to the anchoring effect of N-containing species inhibiting Pd cluster growth. In contrast, catalysis by Pd on carbon blacks without N-containing species achieves less than 10% of the initial hydrogen release amount.

2. Experimental section

2.1. Materials

N-ethylcarbazole (97%) was purchased from Sigma-Aldrich. 3-aminopropyltriethoxysilane (APTES, 99%), palladium (II) chloride (Pd 59–60%) and sodium borohydride (98%) were purchased from Aladdin. Palladium on alumina (5 wt% Pd loading) and ruthenium on alumina (5 wt% Ru loading) were purchased from Alfa Aesar. Sodium chloride (AR) and nitric acid were purchased from Sinopharm Chemical Reagent, Co., Ltd. Super P carbon blacks were purchased from Lizhiyuan Battery Materials Co., Ltd.

2.2. Synthesis of catalysts

For the preparation of C_{HNO3}, 300 mg Super P carbon blacks were dispersed in 30 mL of 6.0 M HNO_3 and then stirred for 4 h under 363 K. The sample was washed with deionized water and separated by filtration. For the preparation of N–C_{HNO3}, 100 mg C_{HNO3} was dispersed in 30 mL deionized water, followed by the addition of 0.1 mL APTES and

sonication for 2 h [29]. The sample was separated by centrifugation and washed with deionized water three times to obtain N–C_{HNO3}. Preparation of N–C was similar, except the adoption of untreated Super P carbon blacks instead of C_{HNO3}. For the preparation of Na_2PdCl_4 solution, a certain amount of $PdCl_2$ and NaCl was dissolved in water in a molar ratio of 1:2 and stirred at 333 K for 1 h, resulted in a solution of Na_2PdCl_4 (0.047 M).

In a typical synthesis of Pd/N–C_{HNO3}, 100 mg N–C_{HNO3} was dispersed in 30 mL deionized water and Na_2PdCl_4 solution (0.047 M, 2.2 mL) was added into N–C_{HNO3} suspension solution under magnetic stirring for 30 min. Subsequently, $NaBH_4$ (0.26 M, 10 mL) was slowly added dropwise under an ice bath into the above mixture and then stirred for 3 h. The sample was separated by centrifugation and washed with deionized water three times and then dried in a vacuum oven at 333 K overnight. The theoretical Pd loading content of Pd/N–C_{HNO3} is 2.20 wt%. Synthesis of 0.5 Pd/N–C_{HNO3} and 2 Pd/N–C_{HNO3} by changing the added amount of Na_2PdCl_4 solution to 1.1 mL or 4.4 mL. Synthesis of Pd/C_{HNO3} and Pd/N–C was similar to Pd/N–C_{HNO3}, except for the use of C_{HNO3} or N–C instead of N–C_{HNO3}. For the synthesis of Pd/C_{HNO3}-APTES, 100 mg Pd/C_{HNO3} was dispersed in 30 mL deionized water, followed by the addition of 0.1 mL APTES, sonication for 2 h, the separation by centrifugation, washing with deionized water three times and then drying in vacuum at 333 K overnight. For all catalysts, the loading ratio of Pd is determined by ICP-OES (Table 1). The actual catalyst loading was found to be close to the theoretical loading, with an error of less than 3%.

2.3. Catalyst characterization

X-ray diffraction (XRD) spectra were collected on Bruker AXS D8 advance at 40 kV and 40 mA with Cu Kα radiation. X-ray photoelectron spectra (XPS) were recorded on a Thermo Scientific K-Alpha system equipped with a dual X-ray source, adopting an Al Kα (1486.6 eV) anode with a hemispherical energy analyzer. Transmission electron microscopy (TEM) images were obtained using an accelerating voltage of 200 kV (JEOL JEM-F200). The Brunner−Emmett−Teller (BET) surface areas were calculated by N_2 adsorption (Micromeritics ASAP 2020 M). The Pd contents of catalyst samples were measured multiple times by an inductively coupled plasma optical emission spectrometer (ICP-OES) (Agilent ICP-OES 730). ^{1}H-NMR was performed on Bruker AVANCEIII 400 M and $CDCl_3$ as solutions.

2.4. Preparation of dodecahydro-N-ethylcarbazole

12H-NEC was obtained through the hydrogenation of NEC. 20 g NEC and 1 g Ruthenium on alumina (5 wt% loading) catalyst loaded into a 100 mL high-pressure reactor with magnetic stirring. After evacuation of 30 min, the reactor was heated to 453 K under a hydrogen pressure of 7 MPa. The reaction was carried out for 8 h with a stirring speed of 600 rpm. The ^{1}H-NMR characterization results indicate a purity of 99.2% for the prepared 12H-NEC (Fig. S1).

2.5. Catalytic dehydrogenation of dodecahydro-N-ethylcarbazole

1.0 mL of liquid 12H-NEC was loaded in a 50-mL three-necked flask reactor with condensation reflux under magnetic stirring. The solution was heated to various temperatures under the purge of argon at 50 mL/min. After the desired temperature was achieved, 28 mg of the prepared catalysts above was added into the reactor. After adding the catalyst, the catalyst in the reactor initiates the catalytic dehydrogenation of 12H-NEC and producing hydrogen. The generated hydrogen is passed through a gas flowmeter (CS200, Sevenstar), and the instantaneous flow rate of hydrogen is recorded at a rate of once per second. Hydrogen release was calculated from the integration of instantaneous flow recorded by the flowmeter and corrected by the ^{1}H-NMR results of the dehydrogenation reaction products. The initial gas flow due to thermal expansion is subtracted. The stepwise kinetic constants (k_1, k_2, k_3) for the dehydrogenation reaction of 12H-NEC were calculated by fitting the dehydrogenation curve. The specific calculation methods are detailed in the Supporting Information. During the cyclic testing, the reaction products were washed with ethyl acetate under argon protection and the catalyst was recovered by centrifugation and then dried in a vacuum oven at 333 K overnight.

Table 1
ICP-OES analysis of loading ratio of Pd in different catalysts.

	Pd/N–C_{HNO3}	Pd/N–C	Pd/C_{HNO3}
Pd loading (wt.%)	2.20	2.18	2.25
	Pd/C_{HNO3}-APTES	0.5 Pd/N–C_{HNO3}	2 Pd/N–C_{HNO3}
Pd loading (wt.%)	2.20	1.08	4.42

2.6. Computational methods

DFT calculations were carried out using projector-augmented wave (PAW) method as implemented in Vienna ab initio simulation package (VASP) [33–36]. The generalized gradient approximation (GGA) of Perdew-Burke-Ernzerhof (PBE) functional was employed to describe the exchange-correlation interaction, and the van der Waals (vdW) correction DFT-D3 proposed by Grimme was chosen to describe the dispersion interaction [37,38]. The plane wave energy cut-off was set as 500 eV, and Gamma centered k-points mesh whose Kmesh-Resolved value was 0.03 2π Å−1 was applied to all calculations. The structures were relaxed until the forces and total energy on all atoms were converged to less than 0.05 eV $Å^{-1}$ and 1×10^{-5} eV. Spin-polarization and dipole correction were also considered in all calculation. A 2-layer slab of Pd (100) was built as matrix and a pyrrole molecule was attached to the bottom of slab to simulate the effect of N-doped carbon. The Gibbs free energy is calculated according to the following formula:

$$\Delta G = \Delta E_{Total} + \Delta E_{ZPE} + \Delta nRT - T\Delta S$$

E_{Tatal} was the total energy, E_{ZPE} was the zero-point energy correction, n was number of molecules, R was molar gas constant, T was temperature and S was entropy.

3. Results and discussion

As schematically illustrated in Fig. 1, the surface of carbon blacks is initially oxidized by nitric acid (denoted as C_{HNO3}), followed by amine-functionalization by APTES (denoted as N–C_{HNO3}). Finally, the uniform distribution of Pd nanoclusters on the surface of N–C_{HNO3} is realized by using Na_2PdCl_4 as the palladium source and sodium borohydride as the reducing agent (denoted as Pd/N–C_{HNO3}). To investigate the effects of

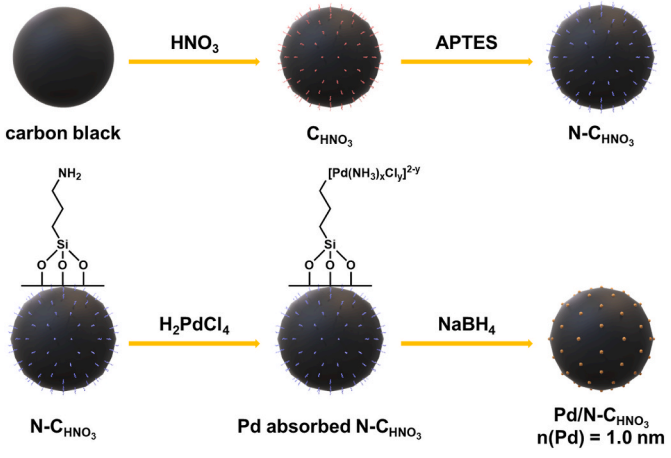

Fig. 1. Schematic illustration of the fabrication of Pd/N–C_{HNO3}.

surface oxidation and amine functionalization of the support in tuning particle size and the distribution of Pd nanoclusters, the formation of Pd on the surface of carbon blacks is also fabricated without prior nitric acid oxidation treatment of carbon blacks (denoted as Pd/N–C_{HNO3}), while the formation of Pd on the surface of C_{HNO3} is fabricated without amine-functionalization of C_{HNO3} (denoted as Pd/C_{HNO3}). To examine the influence of nitrogen doping introduced by amine functional groups separately after the formation of Pd nanoparticles on its catalytic performance, Pd/C_{HNO3}-APTES was synthesized by mixing Pd/C_{HNO3} with APTES followed by sonication. Additionally, it is generally believed that the larger the loading amount of Pd, the larger the particle size [24]. To further investigate the impact of particle size on the catalytic activity of Pd and identify the optimal loading amount of Pd, Pd/N–C_{HNO3} catalysts with 0.5 and 2 times the Pd loading amount (1.1 wt% and 4.4 wt%) were also synthesized for comparison, denoted as 0.5 Pd/N–C_{HNO3} and 2 Pd/N–C_{HNO3}, respectively.

Transmission electron microscopy (TEM) images of Pd/N–C_{HNO3} illustrate that, due to the ultrasmall particle size of Pd nanoclusters, it is hard to directly measure the particle size of Pd nanoclusters (Fig. S2). Therefore, the structures and morphologies of the as-synthesized Pd/N–C_{HNO3} are characterized using high-angle annular dark-field scanning transmission electron microscopy (HAADF-STEM). The presence of Pd nanoclusters on the surface of carbon blacks could be clearly observed (Fig. 2a). The structures and morphologies of catalysts Pd/N–C, Pd/C_{HNO3} and Pd/C_{HNO3}-APTES were characterized using TEM (Fig. 2b–d). All particle sizes of Pd nanoparticles obtained through TEM characterization are listed in Table 4. Among these catalysts, the particle size of Pd nanoclusters in Pd/N–C_{HNO3} is the smallest, with an average diameter of 1.1 nm. The average particle size of Pd in Pd/N–C fabricated without prior treatment of carbon blacks with nitric acid but with amine functionalization is found to be 3.0 nm, and the average particle size of Pd/C_{HNO3} loaded on a support that was only pretreated with nitric acid but not functionalized with amine is approximately 3.9 nm. Hence, it could be concluded that the nitrogen-doped anchoring sites introduced by amine functionalization on the surface of carbon could effectively anchor Pd towards the formation of Pd nanoclusters. Moreover, according to the XPS characterization results (Fig. 3a–b), the proportion of nitrogen elements in the catalyst is listed in Table S2. It can be observed that the nitrogen content in the catalysts Pd/N–C_{HNO3} prepared by functionalization with APTES on C_{HNO3} carrier pre-oxidized with nitric acid then loaded with Pd is higher compared to the catalyst Pd/N–C prepared by APTES functionalization on carbon blacks then loaded with Pd. This further indicates that pre-oxidation of the carrier facilitates the APTES functionalization process. The proposed mechanism of Pd nanoclusters formation is as follows: Initially, nitric acid serves as an oxidant to introduce numerous oxygen-containing functional groups on the surface of the carbon black. These groups facilitate subsequent hydrolysis reactions with Si–OH of APTES, leading to the sufficient incorporation of amine functional groups [39]. In the subsequent reduction step, the amine groups effectively chelate $[PdCl_4]^{2-}$ to form $[Pd(NH_3)_xCl_y]^{2-y}$ and serve as the initial nucleation sites for Pd, and meanwhile on the surface with only oxidized functional groups and lacking nitrogen-functional groups, it is more challenging to anchor the $[PdCl_4]^{2-}$ as the initial nucleation sites for Pd [40–42]. In this process, the nitrogen-doped sites introduced by APTES can effectively prevent the Pd^0 generated by sodium borohydride reduction from being re-oxidized to $Pd^{\delta+}$ [43–45], which is consistent with the results obtained from subsequent XPS characterization analysis.

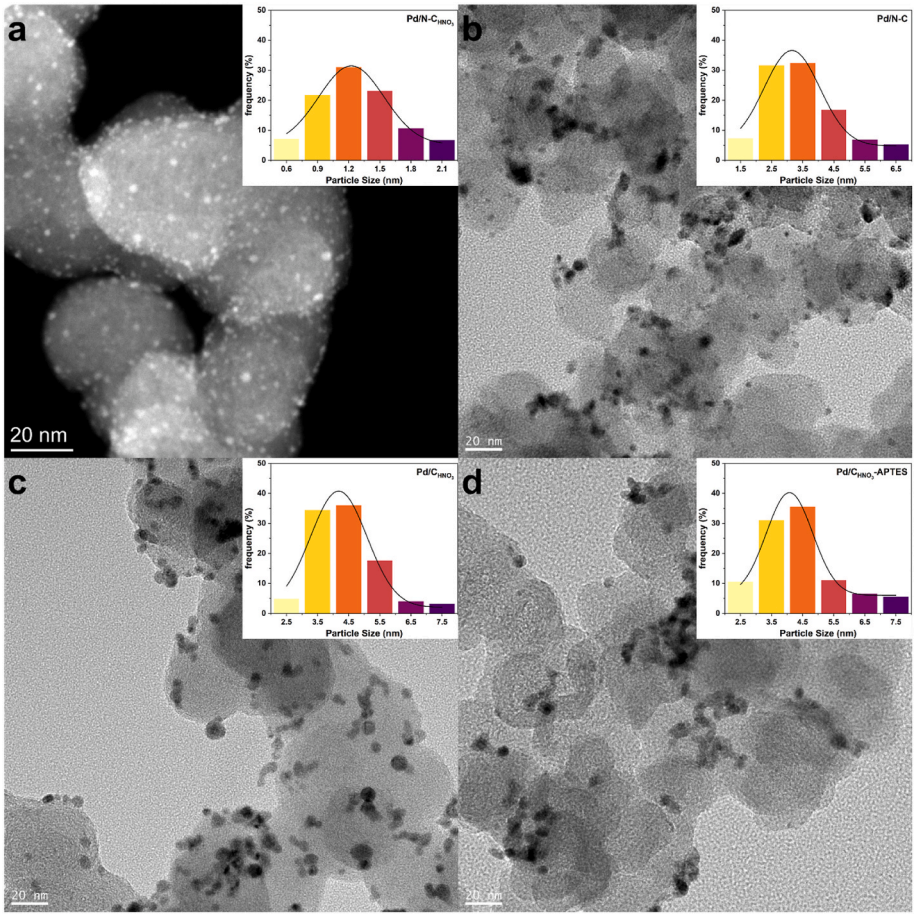

Fig. 2. (a) HAADF-STEM images and corresponding Pd particle size distributions of Pd/N–C_{HNO3} catalysts. (b–d) TEM images and corresponding Pd particle size distributions of Pd/N–C, Pd/C_{HNO3} and Pd/C_{HNO3}-APTES catalysts.

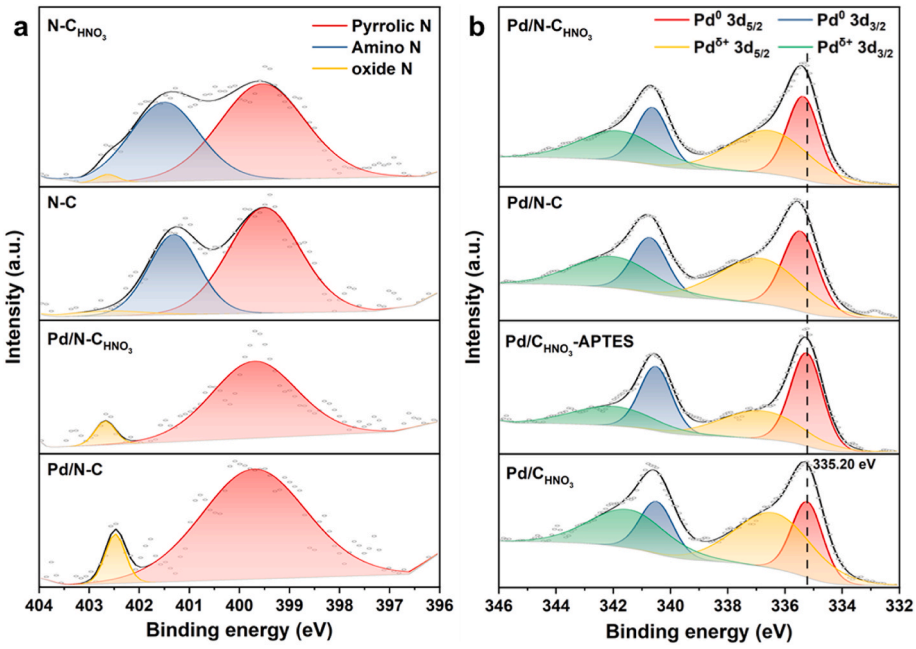

Fig. 3. (a) XPS spectra of N 1s in N–C_{HNO3}, N–C, Pd/N–C_{HNO3} and Pd/N–C. (b) XPS spectra of Pd 3 d in Pd/N–C_{HNO3}, Pd/N–C, Pd/C_{HNO3} and Pd/C_{HNO3}-APTES.

To further demonstrate this mechanism, Pd/C_{HNO3} catalyst is treated by APTES amine functionalization to obtain Pd/C_{HNO3}-APTES, in which the average particle size of Pd is also 3.9 nm, indicating that the introduction of amine after Pd nucleation did not affect the particle size of Pd. X-ray diffraction (XRD) patterns (Fig. S3) demonstrate that both N–C_{HNO3} support and Pd/N–C_{HNO3} catalyst exhibit two typical XRD peaks, corresponding to the (002) and (100) peaks of the carbon material [46] and no discernible characteristic peaks of Pd could be observed, which could be attributed to the ultrasmall size and low amount of Pd in Pd/N–C_{HNO3}. In contrast to Pd/N–C_{HNO3}, a characteristic peak of Pd (100) can be slightly observed in the XRD characterization of Pd/N–C and Pd/C_{HNO3} catalysts at 40.1°. Due to the low loading of Pd the remaining characteristic peaks of Pd are hard to observe in the XRD spectra. This suggests that the Pd particle size in Pd/CA and Pd/CO should be larger than that in Pd/COA. Brunner–Emmett–Teller (BET) surface areas analysis (Table 2) indicates that the introduction of APTES slightly reduces the surface area of the catalyst from 62.52 m^2/g (Pd/C_{HNO3}) to 58.40 m^2/g (Pd/N–C_{HNO3}) and 57.30 m^2/g (Pd/N–C), concurrently there is a slight reduction in the average pore volume from 0.2801 cm^2/g (Pd/C_{HNO3}) to 0.2698 cm^2/g (Pd/N–C_{HNO3}) and 0.2762 cm^2/g (Pd/N–C) attributed to the occupation of carbon surface portions by APTES on the catalyst surface [47].

High-resolution C 1s X-ray photoelectron spectra (XPS) of untreated carbon black and C_{HNO3} (Fig. S4) confirm the successful introduction of oxygen-containing functional groups into carbon black through the nitric acid oxidation process while no detectable peak of N element could be found in high-resolution N 1s XPS spectra of C_{HNO3} (Fig. S5). By comparison, peaks of N elements could be clearly observed in the high-resolution N 1s spectra of N–C_{HNO3} and N–C (Fig. 3a), with binding energies measured at 399.5, 401.6, and 402.6 eV (Table 3), respectively, which could be indexed to pyrrolic N, amino N, and a small amount of oxidized N [48,49]. This result indicates the successful N doping on the surface of carbon black through APTES. Additionally, a distinct Si 2p peak at 102.04 eV was clearly observed for Pd/N–C_{HNO3}, in contrast to the absence of the Si 2p peak for Pd/C_{HNO3} (Fig. S6), further confirming the successful introduction of APTES on the support. Interestingly, after the nucleation of Pd, the peak of amino N in the high-resolution N 1s spectra of Pd/N–C_{HNO3} and Pd/N–C vanished in comparison to N–C_{HNO3} and N–C supports (Fig. 3a), signifying the role of the amino functional group in anchoring Pd. The high-resolution Pd 3 d spectra of Pd/N–C_{HNO3}, Pd/N–C, Pd/C_{HNO3}, and Pd/C_{HNO3}-APTES could be deconvoluted into two sets of doublets (Fig. 3b) that could be attributed to metallic Pd and oxidized Pd. Taking Pd/N–C_{HNO3} as an example, the doublet situated at 335.38 and 340.63 eV correspond to the $3d_{5/2}$ and $3d_{3/2}$ peaks of elemental Pd and the other doublet at 336.51 and 341.82 eV corresponds to the $3d_{5/2}$ and $3d_{3/2}$ peaks of $Pd^{δ+}$ (Table 3) [20]. It's

Table 2
BET analysis of Pd/C_{HNO3}, Pd/N–C and Pd/N–C_{HNO3}.

	Pd/N–C_{HNO3}	Pd/N–C	Pd/C_{HNO3}
Surface area (m^2/g)	58.40	57.30	62.52
Pore volume (cm^2/g)	0.2698	0.2762	0.2801

Table 3
XPS elemental analysis of Pd 3 d in different catalysts.

Sample name	Binding energy (eV)		FWHM (eV)		Atomic percentage (%)	
	Pd^0 $3d_{5/2}$	$Pd^{δ+}$ $3d_{5/2}$	Pd^0 $3d_{5/2}$	$Pd^{δ+}$ $3d_{5/2}$	Pd^0 $3d_{5/2}$	$Pd^{δ+}$ $3d_{5/2}$
Pd/N–C_{HNO3}	335.32	336.51	1.70	3.50	44.21	55.79
Pd/N–C	335.42	336.82	1.90	3.50	43.51	56.49
Pd/C_{HNO3}	335.18	336.36	3.19	3.50	35.61	64.39
Pd/C_{HNO3}-APTES	335.48	337.50	1.66	3.50	50.10	49.90

Table 4
Average Pd particle size in different catalysts.

	Pd/N–C_{HNO3}	Pd/N–C	Pd/C_{HNO3}
particle size (nm)	1.1	3.0	3.9
	Pd/C_{HNO3}-APTES	2 Pd/N–C_{HNO3}	commercial Pd/Al_2O_3
particle size (nm)	3.9	2.5	5.9
	5 cycles Pd/N–C_{HNO3}	5 cycles Pd/N–C	5 cycles Pd/C_{HNO3}
particle size (nm)	1.9	4.2	5.6

worth noting that, after amino functionalization on the carbon black, there is a reduction in the ratio between $Pd^{\delta+}$ and Pd^0. For Pd/C_{HNO3}, the proportion of $Pd^{\delta+}$ is 64.39%, while for Pd/N–C and Pd/N–C_{HNO3}, the $Pd^{\delta+}$ proportions are 56.49% and 55.79%, and in the case of Pd/C_{HNO3}-APTES, the $Pd^{\delta+}$ proportion decreases further to 49.90% (Table 3). The presence of oxidized Pd is induced by the partial oxidation due to its extremely small particle size. In contrast to TEM characterization, Pd nanoclusters loaded on amino groups modified supports Pd/N–C_{HNO3}, despite having smaller particle sizes, exhibit higher Pd^0:$Pd^{\delta+}$ ratios. This suggests that the amino groups within the carbon support have the capability to stabilize highly dispersed Pd^0 nanoparticles, preventing their oxidation. Furthermore, rather than the Pd^0 $3d_{5/2}$ peak of Pd/C_{HNO3}, Pd/N–C_{HNO3} and Pd/N–C exhibit a more obvious positive shift (from +0.15 to +0.3 eV) (Table 3) indicating that amine functionalization plays an effective role in tuning the electronic structure of Pd [25–27]. This change can be primarily attributed to the electron transfer occurring between Pd and the introduced N atoms, which is caused by the higher electronegativity of nitrogen than palladium. In previous research, exploiting such metal-support interactions to modulate the electronic structure of catalytic metal Pd for enhanced catalytic activity is a commonly employed strategy [29–32]. In conclusion, XPS characterization demonstrate the successful introduction of amine functionalization into the catalyst and the manipulation of the electronic structure of the active metal Pd in the catalyst.

Subsequently, the dehydrogenation performance of 12H-NEC under the presence of various catalysts at 453 K is investigated (Fig. 4a). Among all the as-synthesized catalysts, 12H-NEC catalyzed by Pd/N–C_{HNO3} exhibits the highest hydrogen release amount, delivering 5.60 wt% H_2 within 8 h with 100% conversion and 90% selectivity as determined by ^{1}H-nuclear magnetic resonance (^{1}H-NMR) (Fig. 4c). By comparison, the H_2 release amount with Pd/N–C catalyst is only 5.02 wt %, indicating the important role of the pre-treatment of the carbon black by nitric acid oxidation in improving catalytic activity of Pd nanoclusters. Amine functionalization plays a crucial role in anchoring Pd nanoclusters during the nucleation process, while nitric acid oxidation of the carbon black ensures the abundant attachment of subsequent amine groups on the surface of carbon, which promotes the uniform dispersion of Pd nanoclusters in Pd/N–C_{HNO3}, thus contributing to their overall catalytic performance. Interestingly, although Pd/N–C and Pd/N–C_{HNO3} have similar surface areas based on BET results and similar electronic properties of Pd based on XPS results, the catalytic activity of Pd/N–C_{HNO3} is much better than that of Pd/N–C, indicating the smaller particle size of Pd in Pd/N–C_{HNO3} (1.1 nm) than Pd/N–C (3.0 nm) also plays an important role in enhancing its catalytic effect. The H_2 release amount with Pd/C_{HNO3} catalyst is as low as 4.18 wt%, even lower than that catalyzed by commercial Pd/Al_2O_3 catalyst (4.21 wt%). Although Pd/C_{HNO3} has a larger catalyst surface area than Pd/N–C_{HNO3} and Pd/N–C, its catalytic activity is far inferior to that of Pd/N–C_{HNO3} and Pd/N–C, which is mainly due to the largest average particle size of Pd in Pd/C_{HNO3} (3.9 nm) among all the catalysts. Furthermore, in comparison to Pd/N–C_{HNO3} and Pd/N–C that possess a similar Pd^0:$Pd^{\delta+}$ ratio, a lower Pd^0:$Pd^{\delta+}$ ratio could be observed for Pd/C_{HNO3} due to the lack of amino groups to stabilize highly dispersed Pd^0 nanoparticles, which possibly accounts for inferior catalytic activity of Pd/C_{HNO3} than Pd/N–C and Pd/N–C_{HNO3}. This highlights the role of tuning Pd^0:$Pd^{\delta+}$ ratio in optimizing catalytic performance of Pd nanoparticles.

To unravel the effect of amino groups in improving the catalytic effect of Pd, Pd/C_{HNO3} catalyst is treated by APTES for additional amine functionalization to obtain Pd/C_{HNO3}-APTES. The H_2 release amount of 12H-NEC catalyzed by Pd/C_{HNO3}-APTES within 8 h is 4.48 wt%, which is between the value under the catalysis of Pd/C_{HNO3} and Pd/N–C (Fig. 4b). XPS (Fig. S7) revealed that Pd/C_{HNO3}-APTES also exhibited clear interaction between the as-synthesized Pd nanoparticles and the introduced ammine groups, leading to a higher Pd^0 proportion of 50% than that of Pd/N–C. Therefore, although the average particle size of Pd/C_{HNO3}-APTES is the same as the Pd/C_{HNO3} (3.9 nm) but larger than that of Pd/N–C (3.0 nm), its catalytic activity for H_2 release is better than that of Pd/C_{HNO3} and inferior to that of Pd/N–C. The above result directly demonstrates that the introduction of ammine groups is capable of improving catalytic activity of Pd nanoparticles under the same particle

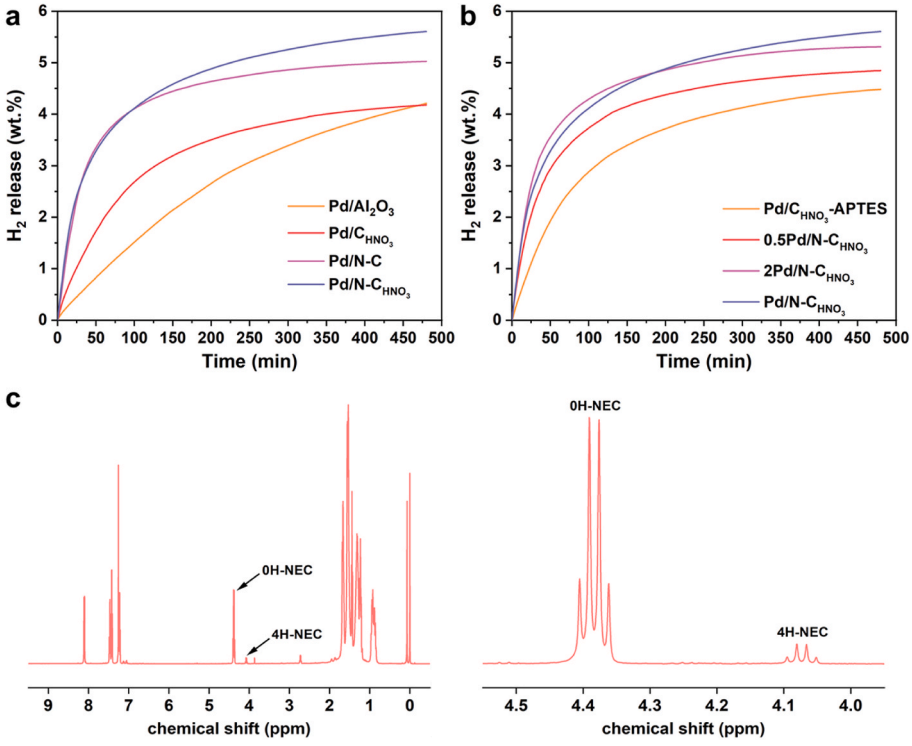

Fig. 4. (a–b) Hydrogen release amount of 12H-NEC dehydrogenation on the Pd/Al_2O_3, Pd/C_{HNO3}, Pd/N–C and Pd/N–C_{HNO3}; Pd/C_{HNO3}-APTES, 0.5 Pd/N–C_{HNO3}, 2 Pd/N–C_{HNO3} and Pd/N–C_{HNO3} at 453 K. (c) ^{1}H-NMR results of 12H-NEC dehydrogenation products under the catalysis of Pd/N–C_{HNO3} in 473 K.

size, indicating that the amount of $Pd^{\delta+}$ species that could hinder the desorption of dehydrogenation products from the catalyst surface should be also well tuned [25]. These experimental findings emphasize the critical role of particle sizes and an optimal Pd^0:$Pd^{\delta+}$ ratio in enhancing the catalytic performance of Pd nanoparticles. To further confirm the optimal Pd loading amount and investigate the effect of particle size of Pd nanoparticles in enhancing the dehydrogenation of 12H-NEC, the loading amounts of Pd nanoclusters of 1.1 wt% and 4.4 wt %, denoted as 0.5 Pd/N–C_{HNO3} and 2 Pd/N–C_{HNO3}, respectively, are also fabricated. TEM images reveal that Pd nanoclusters in 2 Pd/N–C_{HNO3} have a larger average particle size (2.5 nm) than that of Pd/N–C_{HNO3} (1.1 nm) (Fig. S9). The H_2 release amount of 12H-NEC catalyzed by 0.5 Pd/N–C_{HNO3} within 8 h is 4.84 wt%, while this value is only increased to 5.31 wt% for 2 Pd/N–C_{HNO3} that has twice the Pd loading amount (Fig. 4b), both of which are lower than that of Pd/N–C_{HNO3} (5.60 wt%). This provides additional evidence to the key role of particle size of Pd nanoclusters in improving dehydrogenation performance of 12H-NEC.

It is noteworthy that we observed comparable rates of 12H-NEC dehydrogenation catalyzed by Pd/N–C and Pd/N–C_{HNO3} catalysts in the first 80 min of the reaction. However, in the subsequent reaction period, the dehydrogenation rate of 12H-NEC catalyzed by Pd/N–C_{HNO3} became faster than that of Pd/N–C. It is known that the dehydrogenation process of 12H-NEC could be divided into three consecutive first-order reactions [22]. By solving and fitting the following differential equations, the kinetic constants k_1, k_2, and k_3 for the distributional dehydrogenation of 12H-NEC could be obtained (Table S3). For the dehydrogenation curves of 12H-NEC under the catalysis of different catalysts at various temperatures, all the R^2 values of the fittings are larger than 0.99. Consistent with previous research [22], the corresponding k values of three dehydrogenation steps of 12H-NEC under the catalysis of various catalysts at different temperatures exhibit a tendency of $k_1 > k_2 \gg k_3$, indicating that the dehydrogenation step of 4H-NEC to NEC is the rate-controlling step for the complete dehydrogenation of 12H-NEC. Using the obtained kinetic constants, we can derive curves illustrating the concentration changes over time for reactants (12H-NEC), reaction intermediates (8H-NEC, 4H-NEC), and reaction products (NEC) (Fig. S8). It can be observed that under the catalysis of Pd/N–C_{HNO3} and Pd/N–C, the concentrations of intermediate species 8H-NEC and 4H-NEC reach their maximum values at almost the same time in the reaction. at almost the same time, indicating a similar reaction rate in the dehydrogenation of 12H-NEC to form 4H-NEC. However, after 80 min, the concentration of 4H-NEC starts to decrease. This suggests that the predominant step in the reaction system is 4H-NEC → 0H-NEC, and the catalytic abilities of the two catalysts diverge in this rate-determining step. This also explains why after 80 min the dehydrogenation rate of 12H-NEC catalyzed by Pd/N–C_{HNO3} becomes faster than that of Pd/N–C. These results indicate that the Pd/N–C_{HNO3} catalyst can effectively accelerate the rate-determining step in the dehydrogenation of 12H-NEC.

To measure the activation energy of the 12H-NEC dehydrogenation reaction the dehydrogenation performance of 12H-NEC under the catalysis of these catalysts at temperatures ranging from 443 K to 473 K are subsequently investigated (Fig. 5a–c). The apparent activation energy of 4H-NEC → NEC is calculated using the Arrhenius equation by selecting the reaction kinetic constants of the rate-controlling step at different temperatures. As shown in Fig. 5d, the dehydrogenation of 4H-NEC to NEC under the catalysis of Pd/N–C_{HNO3} has the lowest apparent activation energy, which is consistent with its excellent dehydrogenation performance, while Pd/C_{HNO3} has the highest apparent activation energy. Considering the overall dehydrogenation performance of 12H-NEC under the catalysis of various reported catalysts in the literature (Table S1), Pd/N–C_{HNO3} exhibit comparable catalytic activity with the best reported catalyst but with the lowest usage of precious metal.

To evaluate the catalytic stability of Pd/N–C_{HNO3}, Pd/N–C, and Pd/C_{HNO3}, cycling dehydrogenation of 12H-NEC is investigated at a temperature of 463 K. As shown in Fig. 6a, the catalytic performance of Pd/N–C_{HNO3} remains nearly constant during the initial three cycles for 24 h. Even after the fifth cycle for 40 h, a H_2 release amount of 5.49 wt% could still be achieved for 12H-NEC under the catalysis of Pd/N–C_{HNO3}, corresponding to a capacity retention of 96%, which demonstrates the well-

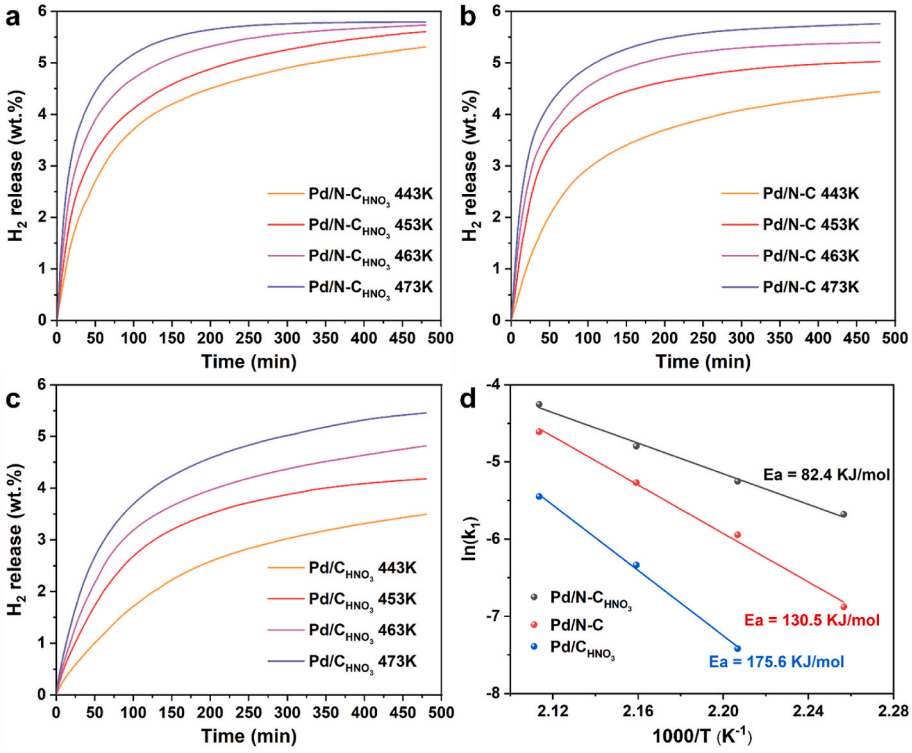

Fig. 5. (a–c) Hydrogen release amount of 12H-NEC dehydrogenation on the Pd/N–C_{HNO3}, Pd/N–C and Pd/C_{HNO3} at 443–473 K. (d) Arrhenius plot (ln k versus 1/T) about Pd/N–C_{HNO3}, Pd/N–C and Pd/C_{HNO3} catalyst.

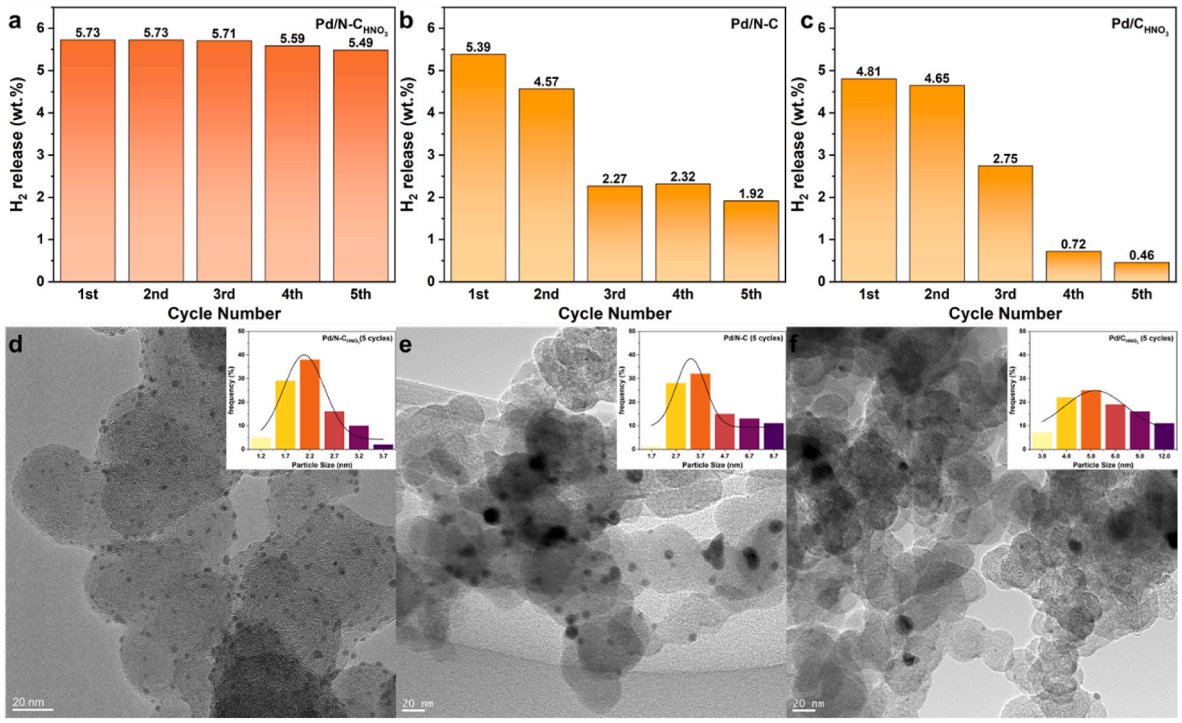

Fig. 6. (a–c) Hydrogen release amount in 5 cycles of 12H-NEC dehydrogenation on the Pd/N–C_{HNO3}, Pd/N–C and Pd/C_{HNO3} at 463 K. (d–f) HADDF-STEM images and corresponding Pd particle size distributions of Pd/N–C_{HNO3}, Pd/N–C and Pd/C_{HNO3} catalyst after 5 cycles.

preserved catalytic effect of Pd/N–C_{HNO3}. In contrast, only 36% of the initial hydrogen release amount could be obtained for 12H-NEC under the catalysis of Pd/N–C after five cycles (Fig. 6b), indicating incomplete dehydrogenation from 12H-NEC to 8H-NEC. Furthermore, the H_2 release amount of 12H-NEC under the catalysis of Pd/C_{HNO3} decays to merely 10% of its initial value after the fifth cycle (Fig. 6c), delivering 0.46 wt% of hydrogen release amount. TEM image (Fig. 6d–f) illustrates that Pd/N–C_{HNO3} catalyst exhibited a well-maintained dispersion of Pd NCs after five cycles, with only a slight increase in the average particle size of Pd nanoclusters from 1.1 nm to 1.9 nm and no evident aggregation. By comparison, significant aggregation and the presence of Pd nanoparticles larger than 10 nm could be observed for both Pd/N–C and Pd/C_{HNO3} catalysts, which accounts for the significant degradation of their catalytic activity. These results confirm that the amine-functionalization of carbon blacks effectively anchors the loaded Pd NCs, and the electronic interactions between Pd and N-containing species effectively inhibit the serious aggregation of Pd nanoclusters during the high-temperature dehydrogenation, thereby contributing to the well-preserved catalytic stability of Pd/N–C_{HNO3}.

To gain further insights into the impact of nitrogen doping on the activity of Pd nanoclusters, theoretical calculations based on density functional theory (DFT) are conducted. The optimized configurations of 12H-NEC, 8H-NEC, 4H-NEC, and NEC are shown in Fig. S11 and the most stable Pd crystal surface, agglomerating, Pd (111), is adopted to simulate the adsorption of the reactant (12H-NEC), intermediate products (8H-NEC and 4H-NEC), and final product (0H-NEC). Considering pyrrolic nitrogen is the main component of N-containing species as determined by XPS characterization, the computational model composed of a pyrrole five-membered ring positioned beneath two layers of Pd is built to unravel the effect of N-doping in improving the catalytic activity of Pd nanoclusters. The changes in Gibbs free energy (ΔG) for the three-step dehydrogenation reaction of 12H-NEC are illustrated in Fig. 7a. Regardless of the presence or absence of nitrogen doping in the support, the dehydrogenation of 12H-NEC was thermodynamically favorable at 453 K. Specifically, when nitrogen doping is introduced in the support, the ΔG values for the three-step dehydrogenation of 12H-NEC are −1.25, −1.57, and −1.12 eV, respectively, delivering a total ΔG of −3.94 eV. In contrast, when nitrogen doping is absent in the support, the ΔG values for the three-step dehydrogenation are −0.64, −1.28, and −0.60 eV, respectively, delivering a total ΔG of −2.52 eV. It is worth noting that each step of the three-step dehydrogenation of 12H-NEC exhibits higher ΔG values on the nitrogen-doped support compared to the non-doped support. Generally, larger absolute ΔG values indicate a more favorable reaction, suggesting that the nitrogen doping in the catalyst support facilitates the dehydrogenation of 12H-NEC on the Pd surface. To further elucidate the reasons behind the ΔG of dehydrogenation reaction change, in-depth investigation of the electronic structure of Pd clusters in the catalyst is conducted. Spin-polarized partial density of states (PDOS) analysis the *d*-band center of the Pd (111) surface shifts from −1.64 eV to −1.53 eV upon nitrogen doping and moves closer to the Fermi level (Fig. 7b) and hence Pd becomes more electron-deficient upon nitrogen doping, which confirms the electron transfer from Pd to N, consistent with our previous XPS results. Interestingly, induced by this phenomenon, the adsorption energies of each reactant species (12H-NEC, 8H-NEC, 4H-NEC, and 0H-NEC) on nitrogen-doped Pd (111) surfaces are found to be higher than those on non-doped Pd (111) surfaces (Fig. 7c). It is worth noting that the adsorption energies of 12H-NEC and 8H-NEC on non-doped Pd (111) surfaces are similar (*i.e.*, 1.50 eV and 1.45 eV, respectively), while their adsorption energies on nitrogen-doped Pd (111) surfaces are significantly increased to 1.55 eV and 2.13 eV, respectively. This validates the important role of nitrogen doping in tuning the electronic structure of Pd nanoclusters and hence the superior adsorption of reactant species of 12H-NEC on the surface of Pd nanoclusters, which could effectively facilitate the catalytic role of Pd nanoclusters in enhancing the hydrogen desorption performance of 12H-NEC.

4. Conclusion

In this study, a highly active Pd/N–C_{HNO3} catalyst with a low Pd loading amount of 2.2 wt% supported on amine-functionalized carbon black is developed to realize the efficient dehydrogenation of 12H-NEC.

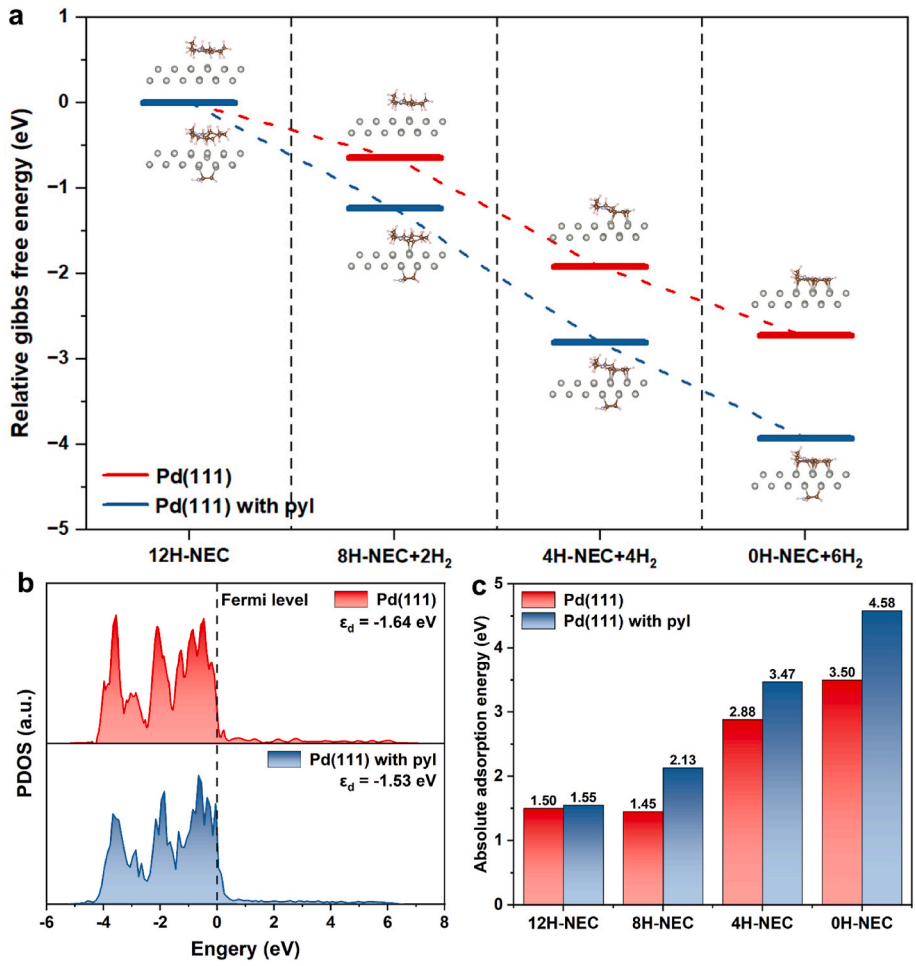

Fig. 7. (a) The Gibbs free energy (eV) changes from 12H-NEC dehydrogenation to NEC on pure Pd (111) surfaces and pyrrolic-N modified Pd (111) surfaces at 453 K. (b) Projected density of states (PDOS) for the surface atoms of pure Pd (111) surfaces and pyrrolic-N modified Pd (111) surface. (c) Absolute adsorption energies (eV) of 12H-NEC, 8H-NEC, 4H-NEC and NEC on pure Pd (111) surfaces and pyrrolic-N modified Pd (111) surfaces at 453 K.

The average particle size of thus-formed Pd nanoclusters is approximately 1.1 nm, which is the most appropriate particle size of Pd catalyst for promoting the hydrogen desorption of 12H-NEC. Moreover, the *d*-band center of the Pd (111) surface shifts from −1.64 eV to −1.53 eV and moves closer to the Fermi level induced by the nitrogen doping in the carbon black, which leads to the electron-deficient structure of thus-formed Pd nanoclusters owing to the electron transfer from Pd to N atoms and uniform distribution of Pd nanoclusters inside of carbon blacks. More importantly, induced by this electron transfer between Pd and N atoms, the thus-tuned Pd^0:$Pd^{\delta+}$ ratio enhances the adsorption of reactant species of 12H-NEC on the surface of Pd nanoclusters, which could effectively facilitate the catalytic role of Pd nanoclusters in enhancing the hydrogen desorption performance of 12H-NEC. As a result, each step of the dehydrogenation of 12H-NEC under the catalysis of Pd nanoclusters on the nitrogen-doped support exhibits lower ΔG values compared to the non-doped support, which directly demonstrates the important role of the nitrogen doping in the catalyst support in improving the dehydrogenation of 12H-NEC on the Pd surface. Therefore, using a low precious metal loading amount (0.12 mol%), a hydrogen release capacity of 5.60 wt% with 100% conversion and a selectivity of 90% could be obtained for 12H-NEC under the catalysis of Pd nanoclusters supported on amine-functionalized carbon black at 453 K for 8 h. Our work clearly demonstrates the important role of particle size and electronic structure in improving the catalytic effect of Pd catalyst during hydrogen desorption of 12H-NEC and sheds light on the catalyst design strategy for further reducing the usage of precious metals.

Data availability

Data will be made available on request.

CRediT authorship contribution statement

Yumo Li: Writing – original draft, Validation, Investigation, Formal analysis, Data curation. **Jikai Ye:** Investigation, Formal analysis, Data curation. **Tian Xu:** Investigation, Validation. **Guanglin Xia:** Writing – review & editing, Writing – original draft, Supervision, Investigation, Formal analysis, Conceptualization. **Xuebin Yu:** Writing – review & editing, Validation, Supervision.

Declaration of competing interest

The authors declare that they have no known competing financial interests or personal relationships that could have appeared to influence the work reported in this paper.

Acknowledgements

This work was financially supported by the National Key R&D Program of China (No. 2020YFA0406204), the National Natural Science Foundation of China (22279020, 22109026, 51971065, 51901045,

U2130208, and 52071156), the Science and Technology Commission of Shanghai Municipality (No. 21ZR1407500 and 23ZR1406500), and the Innovation Program of Shanghai Municipal Education Commission (2019–01-07–00-07-E00028).

Appendix A. Supplementary data

Supplementary data to this article can be found online at https://doi.org/10.1016/j.ijhydene.2024.03.367.

References

[1] Shaner MR, Atwater HA, Lewis NS, McFarland EW. A comparative technoeconomic analysis of renewable hydrogen production using solar energy. Energy Environ Sci 2016;9:2354–71.
[2] Zhang X, Sun Y, Ju S, Ye J, Hu X, Chen W, Yao L, Xia G, Fang F, Sun D, Yu X. Solar-driven reversible hydrogen storage. Adv Mater 2023;35:2206946.
[3] Lahnaoui A, Wulf C, Heinrichs H, Dalmazzone D. Optimizing hydrogen transportation system for mobility by minimizing the cost of transportation via compressed gas truck in North Rhine-Westphalia. Appl Energy 2018;223:317–28.
[4] Okunlola A, Giwa T, Di Lullo G, Davis M, Gemechu E, Kumar A. Techno-economic assessment of low-carbon hydrogen export from western Canada to Eastern Canada, the USA, the Asia-Pacific, and Europe. Int J Hydrogen Energy 2022;47:6453–77.
[5] Lei Y, Hosseini E, Liu L, Scholes CA, Kentish SE. Internal polymeric coating materials for preventing pipeline hydrogen embrittlement and a theoretical model of hydrogen diffusion through coated steel. Int J Hydrogen Energy 2022;47:31409–19.
[6] Timmerberg S, Kaltschmitt M. Hydrogen from renewables: supply from North Africa to central Europe as blend in existing pipelines – Potentials and costs. Appl Energy 2019;237:795–809.
[7] Zhang Y, Wang J, Zhou F, Liu J. An effective strategy for hydrogen supply: catalytic acceptorless dehydrogenation of N-heterocycles. Catal Sci Technol 2021;11:347–99.
[8] Yadav V, Sivakumar G, Gupta V, Balaraman E. Recent advances in liquid organic hydrogen carriers: an alcohol-based hydrogen economy. ACS Catal 2021:14712–26.
[9] Wang C, Astruc D. Recent developments of nanocatalyzed liquid-phase hydrogen generation. Chem Soc Rev 2021;50:3437–84.
[10] Tan KC, He T, Chua YS, Chen P. Recent advances of catalysis in the hydrogenation and dehydrogenation of N-heterocycles for hydrogen storage. J Phys Chem C 2021;125:18553–66.
[11] Zhou L, Sun L, Xu L, Wan C, An Y, Ye M. Recent developments of effective catalysts for hydrogen storage Technology using N-ethylcarbazole. Catalysts 2020;10:648.
[12] Sievi G, Geburtig D, Skeledzic T, Bösmann A, Preuster P, Brummel O, Waidhas F, Montero MA, Khanipour P, Katsounaros I, Libuda J, Mayrhofer KJJ, Wasserscheid P. Towards an efficient liquid organic hydrogen carrier fuel cell concept. Energy Environ Sci 2019;12:2305–14.
[13] Clot E, Eisenstein O, Crabtree RH. Computational structure-activity relationships in H_2 storage: how placement of N atoms affects release temperatures in organic liquid storage materials. Chem Commun 2007:2231–3.
[14] Tan KC, He T, Chua YS, Chen P. Recent advances of catalysis in the hydrogenation and dehydrogenation of N-heterocycles for hydrogen storage. J Phys Chem C 2021;125:18553–66.
[15] Oh, Jeong K, Kim TW, Kwon H, Han JW, Park JH, Suh YW. 2-(N-Methylbenzyl) pyridine: a potential liquid organic hydrogen carrier with fast H_2 release and stable activity in consecutive cycles. ChemSusChem 2018;11:661–5.
[16] Yook H, Jeong K, Hwang J, Park JH, Han JW. Roles of bridge carbon and heteroatom during the dehydrogenation reaction of dicyclohexylmethane derivatives on Pd and Pt catalysts for liquid organic hydrogen carrier. Appl Catal, B 2024;342:123394.
[17] Lee J, Park BG, Sung K, Lee H, Kim J, Nam E, Han JW, An K. Reversible Pd catalysts supported on hierarchical titanate nanosheets for an N-Methylindole-Based liquid organic hydrogen carrier. ACS Catal 2023;13:13691–703.
[18] Mejuto C, Ibáñez-Ibáñez L, Guisado-Barrios G, Mata JA. Visible-light-promoted iridium(III)-Catalyzed acceptorless dehydrogenation of N-heterocycles at room temperature. ACS Catal 2022;12:6238–45.
[19] Yang M, Han C, Ni G, Wu J, Cheng H. Temperature controlled three-stage catalytic dehydrogenation and cycle performance of perhydro-9-ethylcarbazole. Int J Hydrogen Energy 2012;37:12839–45.
[20] Eblagon KM, Tam K, Tsang SCE. Comparison of catalytic performance of supported ruthenium and rhodium for hydrogenation of 9-ethylcarbazole for hydrogen storage applications. Energy Environ Sci 2012;5:8621–863.
[21] Morawa Eblagon K, Tam K, Yu KMK, Zhao S, Gong X, He H, Ye L, Wang L, Ramirez-Cuesta AJ, Tsang SC. Study of catalytic sites on ruthenium for hydrogenation of N-ethylcarbazole: implications of hydrogen storage via reversible catalytic hydrogenation. J Phys Chem C 2010;114:9720–30.
[22] Yang M, Dong Y, Fei S, Ke H, Cheng H. A comparative study of catalytic dehydrogenation of perhydro-N-ethylcarbazole over noble metal catalysts. Int J Hydrogen Energy 2014;39:18976–83.
[23] Wang B, Chang T, Jiang Z, Wei J, Fang T. Component controlled synthesis of bimetallic PdCu nanoparticles supported on reduced graphene oxide for dehydrogenation of dodecahydro-N-ethylcarbazole. Appl Catal, B 2019;251:261–72.
[24] Dong C, Gao Z, Li Y, Peng M, Wang M, Xu Y, Li C, Xu M, Deng Y, Qin X, Huang F, Wei X, Wang Y, Liu H, Zhou W, Ma D. Fully exposed palladium cluster catalysts enable hydrogen production from nitrogen heterocycles. Nat Catal 2022;5:485–93.
[25] Meng H, Yang Y, Shen T, Yin Z, Zhang J, Yan H, Wei M. Highly efficient hydrogen production from dehydrogenation reaction of nitrogen heterocyclesvia Pd0-Pdδ+ synergistic catalysis. ACS Catal 2023;13:9234–44.
[26] Lee Y, Ahn JH, Shin S, Jung S, Park H, Cho Y, Lee D, Kong H, Lee JH, Song H. Metal-nitrogen intimacy of the nitrogen-doped ruthenium oxide for facilitating electrochemical hydrogen production. Appl Catal, B 2022;303:120873.
[27] Li Z, Chen Y, Ji S, Tang Y, Chen W, Li A, Zhao J, Xiong Y, Wu Y, Gong Y, Yao T, Liu W, Zheng L, Dong J, Wang Y, Zhuang Z, Xing W, He C, Peng C, Cheong W, Li Q, Zhang M, Chen Z, Fu N, Gao X, Zhu W, Wan J, Zhang J, Gu L, Wei S, Hu P, Luo J, Li J, Chen C, Peng Q, Duan X, Huang Y, Chen X, Wang D, Li Y. Iridium single-atom catalyst on nitrogen-doped carbon for formic acid oxidation synthesized using a general host–guest strategy. Nat Chem 2020;12:764–72.
[28] Jin H, Liu X, Chen S, Vasileff A, Li L, Jiao Y, Song L, Zheng Y, Qiao S. Heteroatom-doped transition metal electrocatalysts for hydrogen evolution reaction. ACS Energy Lett 2019;4:805–10.
[29] Cui Y, Zhao M, Zou Y, Zhang J, Han J, Wang Z, Jiang Q. Ultrasmall AuPd nanoclusters on amine-functionalized carbon blacks as high-performance bi-functional catalysts for ethanol electrooxidation and formic acid dehydrogenation. J Energy Chem 2022;68:556–63.
[30] Warczinski L, Hättig C. How nitrogen doping affects hydrogen spillover on carbon-supported Pd nanoparticles: new insights from DFT. J Phys Chem C 2021;125:9020–31.
[31] Warczinski L, Hu B, Eckhard T, Peng B, Muhler M, Hattig C. Anchoring of palladium nanoparticles on N-doped mesoporous carbon. Phys Chem Chem Phys 2020;22:21317–25.
[32] Bi QY, Lin JD, Liu YM, He HY, Huang FQ, Cao Y. Dehydrogenation of formic acid at room temperature: boosting palladium nanoparticle efficiency by coupling with pyridinic-nitrogen-doped carbon. Angew Chem, Int Ed 2016;55:11849–53.
[33] Jiang H, Liu L, Zhao K, Liu Z, Zhang X, Hu S. Effect of pyridinic- and pyrrolic-nitrogen on electrochemical performance of Pd for formic acid electrooxidation. Electrochim Acta 2020;337:135758.
[34] Blochl PE. Projector augmented-wave method. Phys Rev B 1994;50:17953–79.
[35] Kresse G, Hafner J. Ab-initio molecular-dynamics simulation of the liquid-metalamorphous-semiconductor transition in germanium. Phys Rev B 1994;49:14251–69.
[36] Kresse G, Furthmüller J. Efficiency of ab-initio total energy calculations for metals and semiconductors using a plane-wave basis set. Comput Mater Sci 1996;6:15–50.
[37] John PP, Kieron B, Matthias E. Generalized gradient approximation made simple. Phys Rev Lett 1996;77:3865.
[38] Grimme S, Antony J, Ehrlich S, Krieg H. A consistent and accurate ab initio parametrization of density functional dispersion correction (DFT-D) for the 94 elements H-Pu. J Chem Phys 2010;132:154104.
[39] Fan B, Zhou H, Wang Y, Zhao Z, Ren S, Xu L, Wu J, Yan H, Gao Z. Surface siloxane-modified silica materials combined with metal–organic frameworks as novel MALDI matrixes for the detection of low-MW compounds. ACS Appl Mater Interfaces 2020;12:37793–803.
[40] Kumar KPA, Alduhaish O, Adil SF, Pumera M. Grafting of Pd on covalently and noncovalently modified N-doped graphene for electrocatalysis. Adv Mater Interfac 2022;9:2102317.
[41] Arrigo R, Schuster ME, Xie Z, Yi Y, Wowsnick G, Sun LL, Hermann KE, Friedrich M, Kast P, Hävecker M, Knop-Gericke A, Schlögl R. Nature of the N–Pd interaction in nitrogen-doped carbon nanotube catalysts. ACS Catal 2015;5:2740–53.
[42] Deng M, Yang A, Ma J, Yang C, Cao T, Yang S, Yao M, Liu F, Wang X, Cao J. Enhanced catalytic performance of N-doped carbon sphere-supported Pd nanoparticles by secondary nitrogen source regulation for formic acid dehydrogenation. ACS Appl Mater Interfaces 2022;14:18550–60.
[43] Xu X, Li Y, Gong Y, Zhang P, Li H, Wang Y. Synthesis of palladium nanoparticles supported on mesoporous N-doped carbon and their catalytic ability for biofuel upgrade. J Am Chem Soc 2012;134:16987–90.
[44] Wei Y, Zhang X, Luo Z, Tang D, Chen C, Zhang T, Xie Z. Nitrogen-doped carbon nanotube-supported Pd catalyst for improved electrocatalytic performance toward ethanol electrooxidation. Nano-Micro Lett 2017;9:28.
[45] Murugesan B, Pandiyan N, Arumugam M, Sonamuthu J, Samayanan S, Cai Y, Yao J, Mahalingam S. Fabrication of palladium nanoparticles anchored polypyrrole functionalized reduced graphene oxide nanocomposite for antibiofilm associated orthopedic tissue engineering. Appl Surf Sci 2020;510:145403.
[46] He Z, Dong B, Wang W, Yang G, Cao Y, Wang H, Yang Y, Wang Q, Peng F, Yu H. Elucidating interaction between palladium and N-doped carbon nanotubes: effect of electronic property on activity for nitrobenzene hydrogenation. ACS Catal 2019;9:2893–901.
[47] Shang Y, Cao Z, Chen H, Sun Y, Yao J, Yang L, Qi D, Ziener U. Influence of synthesis parameters on particle properties and catalytic activity of rice roll-like Au/SiO_2 nanocatalysts prepared in inverse miniemulsions. Colloids Surf, A 2018;537:1–12.
[48] Zheng J, Ju S, Xia G, Pan H, Yu X. Co-construction of solid solution phase and void space in yolk–shell $Fe_{0.4}Co_{0.6}S$@N-doped carbon to enhance cycling capacity and rate capability for aluminum-ion batteries. ACS Appl Mater Interfaces 2022;14:8076–85.
[49] Yao L, Ju S, Yu X. Rational surface engineering of MXene@N-doped hollow carbon dual-confined cobalt sulfides/selenides for advanced aluminum batteries. J Mater Chem A 2021;9:16878–88.